Available online at www.sciencedirect.com
SCIENCE DIRECT
International Journal of Mass Spectrometry 252 (2006) 73–78
International Journal of Mass Spectrometry
www.elsevier.com/locate/ijms

Short communication

Velocity map imaging mass spectrometry

Myung Hwa Kim [a,b], Brian D. Leskiw [b,1], Lei Shen [b], Arthur G. Suits [a,b,*]

[a] Department of Chemistry, Stony Brook University, Stony Brook, NY 11794, United States
[b] Department of Chemistry, Wayne State University, Detroit, MI 48202, United States

Received 10 October 2005; received in revised form 19 January 2006; accepted 20 January 2006
Available online 28 February 2006

Abstract

We demonstrate an alternative mass spectrometric technique, Velocity map imaging mass spectrometry, which combines transverse deflection by short, pulsed electric fields with velocity map imaging in a single stage reflectron to achieve spatially resolved mass dispersion. In this simple configuration, ions are clearly separated according to their mass-to-charge ratio through the transverse deflection of the ions perpendicular to the flight direction. In this communication, we demonstrate the technique with the simultaneous detection of Xe isotopes spatially dispersed on a position sensitive detector, showing a mass resolution greater than 600 and dynamic range $>10^3$. The approach has potential applications in tandem mass spectrometry and a variety of dynamics studies.
© 2006 Elsevier B.V. All rights reserved.

Keywords: Velocity map imaging mass spectrometry; Spatial mass dispersion; Pulsed deflection; Xe isotope

1. Introduction

Mass spectrometry is revolutionizing the study of complex molecules, and anticipated advances in proteomics now hinge upon the central contributions of mass spectrometric methods [1,2]. Of the various types of mass spectrometers, only those designs utilizing magnetic sector technology have been successful in the simultaneous detection [3,4] of spatially resolved ions of different masses. Imaging based simultaneous detection offers unique advantages over other time or frequency domain mass spectrometers such as time-of-fight mass (TOFMS), ion trap mass (ITMS), and Fourier transform ion cyclotron resonance mass spectrometers (FT-ICRMS). In a spatially dispersive mode the duty cycle of measurement can be effectively increased owing to the multiplexing advantage, shot-to-shot fluctuations are minimized, and, in this case, kinetic energy and mass may be measured simulatenously [5].

Simultaneous multiple ion monitoring at high resolution has been readily achieved over the years using double focusing EB (eletrostatic energy analyzer and magnetic sector) mass spectrometers in the Mattauch–Herzog geometry [6]. However, one disadvantage of this arrangement is the location of the detector system, in that it must be located at the plane of focus at the magnet exit. Detector technology development has thus played a crucial role in efforts to adapt this multiplexing ion detection capability since the photographic plate was first incorporated by Thomson [3] and Aston [4] in the earliest days of the history of mass spectrometry. More recently, various types of array detectors such as microchannel plate detector arrays, multiple-collector detector arrays, and integrated array systems have been successfully applied with mass spectrometry for the simultaneous detection of multiple ions of different mass-to-charge (m/z) values [5,7,8]. On the other hand, only a few research groups [9,10] have concentrated on developing instrumentation exploiting spatial separation as well as simultaneously multiplexing different masses beyond the magnetic sector approaches. The latter allows very high mass resolution and sensitivity at the price of expensive equipment and complicated operation.

Ion imaging techniques [11–13] have emerged as a powerful means of achieving simultaneous detection of the complete product velocity distribution for ions of a given mass, and these approaches have also been extended to multimass detection strategies [10,14]. We have very recently reported the first demonstration of velocity map ion imaging in a reflectron con-

* Corresponding author. Tel.: +1 313 577 9008; fax: +1 313 577 8822.
E-mail address: asuits@chem.wayne.edu (A.G. Suits).
[1] Present address: Department of Chemistry, Youngstown State University, Youngstown, OH 44555, United States.

1387-3806/$ – see front matter © 2006 Elsevier B.V. All rights reserved.
doi:10.1016/j.ijms.2006.01.030

figuration and the simultaneous detection of multiplex fragments in the vibrationally mediated photodissociation of ions to obtain the full velocity distributions and branching fractions for competitive dissociation pathways [14,15].

In this communication, we demonstrate a simple alternative approach termed velocity map imaging mass spectrometry (VMIMS). The objective of the present study is to demonstrate this spatially resolved mass dispersion in a compact pulsed deflection configuration. This is achieved without a conventional magnetic sector or electric sector by coupling pulsed deflection with the velocity map ion imaging technique in a single-stage reflectron. In this simple illustration of the technique, ions are created in an atomic beam by photoionization and accelerated toward a single stage reflectron. Just before the ion packets reach the deflection plates, a short voltage pulse is applied orthogonal to the ion flight direction and it is turned off before they exit from deflection region. At this moment, ions receive a transverse momentum impulse for different pulse durations, resulting in slightly mass-dependent spatial separation along the transverse direction. As the altered trajectories propagate through the single stage reflectron, the off-axis spatial separation of each ion is then projected onto an imaging detector, and it embodies the original mass spectrum. Ion trajectory simulations using SIMION 7.0 [16] were performed to optimize the focusing elements in developing the technique, and some of these results are also shown to illustrate performance of the instrument. As one of model systems, in this study we use a xenon atomic beam, with its nine naturally occuring isotopes, to characterize the performance of the instrument.

2. Experimental setup

The general design of the reflectron velocity map imaging mass spectrometer was previously reported, as shown in Fig. 1, and only a brief description follows [14,15]. The apparatus consists of a source chamber, an ion optic acceleration assembly, orthogonal deflection plates, a single stage reflectron, and a MCP/phosphor detector. Briefly, a pulsed supersonic atomic beam of 10% xenon in helium is made by expanding the mixture through a Piezoelectric driven pulsed nozzle into vacuum at 10 Hz with pulse width of 250 μs and an absolute backing pressure of 1.3 atm. Following expansion, the atomic beam is skimmed twice and intercepted by a focused laser beam ($f \sim 20$ cm) where resonance enhanced multiphoton ionization (REMPI) is employed. The operating pressures were maintained at $\sim 1.0 \times 10^{-5}$ Torr in the source chamber and at 5×10^{-8} Torr in the main chamber. The ionization laser is formed by frequency doubling the output of a dye laser pumped by a Nd:YAG laser. Typical output power for the doubled dye laser beam entering the chamber is 1.5 mJ/pulse and accurate wavelength calibration is achieved using a wavemeter (Coherent WaveMaster). The Xe isotopes are ionized by the following (2 + 1) resonance enhanced multiphoton ionization (REMPI) scheme:

$$\mathrm{Xe}\ 5p^6(1s) \xrightarrow{2h\nu} \mathrm{Xe}\ 5p^5(^2P^0_{3/2})6s \xrightarrow{h\nu} \mathrm{Xe}^+ \text{ at } 33053.77\ \mathrm{cm}^{-1}$$

Following ionization, which occurs at a specific position between the repeller plate and extractor lens, the Xe ions are accelerated along the central axis of the apparatus through the multi-lens velocity mapping assembly (4000/3200/1755 V/ground), while maintaining the desired velocity mapping conditions. After passing a field free region, the Xe ion packets enter into a defection region housing a pair of plates (10 cm long, 5 cm spacing) with opposite polarity. Following a 750 ns, ±125 V deflection pulse created by a commercial high voltage pulser (DEI, PVX-4150) at 8.985 μs after the laser firing, the trajectory of the Xe ion cloud proceeds slight off-axis and the masses are spatially separated along a line of the direction of the applied pulsed field. The degree of spatial separation on the detector is effectively controlled through timing delay, and width and magnitude of the voltage pulse applied to the deflector. The relative timing of the pulsed atomic beam, laser, deflection plates, and detector was controlled by a delay generator (BNC 555). Following deflection, the Xe ions are redirected by the retarding potential of the reflectron, so Xe isotope ions of different mass-to-charge ratio striking a 120 mm position sensitive dual MCP/P-47 phosphor detector (Burle Co.) are spatially dispersed. Owing to the extended flight time following the deflection pulse, the ion separation is easily controlled. A high voltage pulse 6.1 μs in duration (2.0/1.15 kV bias) using a commercial high voltage pulser (DEI, PVX-4140) is applied to the MCP for the time gate of the Xe isotopes at the same time. An image of the spatially resolved mass dispersion of Xe isotopes is recorded by a CCD camera (Sony, XT-ST50) in conjunction with the IMACQ megapixel imaging program [17] recently developed by our group, which permits real-time event-counting and centroiding of the ion spots. The signals were typically accumulated for 10,000 laser shots for each data set.

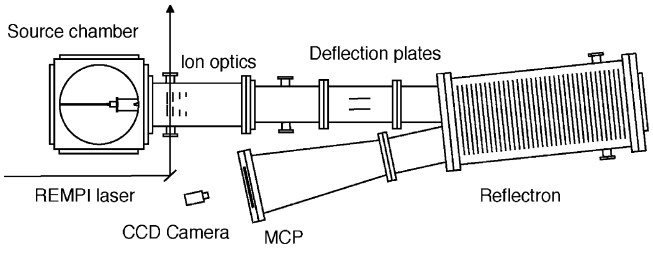

Fig. 1. Schematic view of the velocity map imaging mass spectrometer apparatus.

3. Results and discussion

3.1. Mathematical description

The basic layout of the key components of our instrument is shown schematically to explore the principle of the spatial mass dispersion in more detail in Fig. 2. The ion optics consist of four open electrodes with different aperture sizes and the distances between them are given by s, d_1, and d_2, respectively. The electric field strengths are given by E_s, E_{d_1}, and E_{d_2}, respectively. From the birthplace of the ions, ions with initial energy, U_0, can be

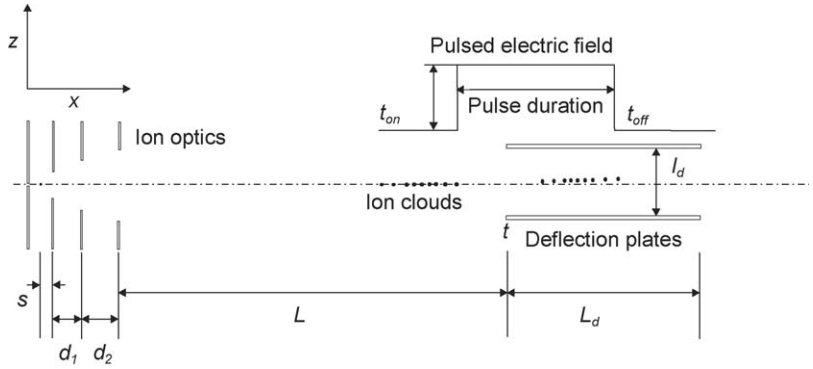

Fig. 2. The basic layout of the key components of our instrument showing the principle of spatial mass dispersion along the transverse direction.

accelerated to a value, U, which is independent of mass m, but dependent on U_0, s, and q.

$$U = U_0 + qsE_s + qd_1E_{d_1} + qd_2E_{d_2} \tag{1}$$

The time-of-flight at the field free region is then given by

$$t = t_s + t_{d_1} + t_{d_2} + t_L \tag{2}$$

where each term is readily shown to be [18,19]

$$t_s = \frac{\sqrt{2m(U_0 + qE_s)}}{qE_s} \tag{3}$$

$$t_d = t_{d_1} + t_{d_2} = \frac{\sqrt{2m}}{qE_{d_2}}[U^{1/2} - (U_0 + qsE_s + qd_2E_{d_2})] + \frac{\sqrt{2m}}{qE_{d_2}}[U^{1/2} - (U_0 + qsE_s + qd_1E_{d_1})] \tag{4}$$

$$t_L = L\sqrt{\frac{m}{2qU}} \tag{5}$$

When the leading edge of the ion cloud reaches some point just before deflection plates, a pulsed electric field is applied in a direction perpendicular to the initial ion flight direction. At this time, the pulsed electric field is very short so that the electric field is turned off before any ions leave the deflection plate region. Under this condition, assuming simple transverse electrostatic deflection and no acceleration effects of transition fields when the ions enter deflection plates, the transverse velocity (v_z) of ions is simply described by the following equation [20]:

$$v_z = \int_t^{t_{\text{off}}} \frac{ql_dE_z}{m}\,\mathrm{d}t = \frac{ql_dE_z}{m}(t_{\text{off}} - t) \tag{6}$$

Here, m is the mass of the ion, E_z the transverse electric field strength, l_d the distance between two deflection plates, q the charge of ion, t the time necessary for the ion to reach the entrance of deflection plates, and t_{off} is the turn-off time of the pulsed electric field. The difference in time, $t_{\text{off}} - t$, is equal to the pulse duration which the ion experiences the transverse field. Since the time of flight in the field free region is proportional to the square root of the mass, the time t in the equation is different for different masses. By substituting of Eq. (2) into Eq. (6), the transverse velocity of the ions arising from the pulsed electric field can be rewritten in terms of the ion masses.

$$v_z = \frac{\alpha}{m} + \frac{\beta}{\sqrt{m}} \tag{7}$$

where α and β are constants. The first term is related to the constant momentum pulse, when the range of time within the deflection region is independent of mass, while the second term represents the contribution of the projection of the initial time dispersion along the flight path direction into the transverse direction.

Eqs. (6) and (7) imply that two factors strongly influence the ultimate spatial mass resolution, the transverse velocity distribution and the spread in the deflection pulse duration. The transverse velocity resolution ($\Delta v_z/v_z$) which is closely correlated with the spatial mass resolution on the detector is primarily limited by small difference in fight times of ions entering into deflection plates for ions of the same mass due to the initial energy distributions. The latter highly depends on the spatial distribution of the ion cloud in deflection region along the transverse direction. The transverse velocity of the ions can be further transformed into the transverse distance of the ion on the detector, s_z, assuming that the reflectron only extends the total flight path under the homogeneous electric field:

$$s_z = \int_{t_{\text{off}}}^{t_a} v_z\,\mathrm{d}t = \int_{t_{\text{off}}}^{t_a} \frac{ql_dE_z}{m}(t_{\text{off}} - t)\,\mathrm{d}t = \frac{ql_dE_z}{2m}(2t_{\text{off}} - t_at_{\text{off}}^2 - t_a^2) \tag{8}$$

If the arrival time (t_a) on the detector is simply proportional to the square root of the mass, the displacement of the ion along the transverse direction on the detector plane can be approximately described as

$$s_z \approx A + \frac{B}{m} + \frac{C}{\sqrt{m}} \tag{9}$$

where A, B, and C are constants. In Eq. (9), it is apparent that different ions hitting on the detector can be spatially separated according to two mass-dependent contribution terms. It should be noted that the range of different masses that can be detected simultaneously depends on the difference in length between the first field free region and the deflection plates, the size of detector in the transverse axis, and mass values. The first factor is governed by $(L - L_d)/L$.

The difference in displacement, Δs_z, that separates adjacent masses between m and $m+1$, is

$$\Delta s_z \approx \frac{B}{m(m+1)} + \frac{C(\sqrt{m+1} - \sqrt{m})}{\sqrt{m(m+1)}} \quad (10)$$

As shown in Eq. (10), the mass dispersion between adjacent masses is small for higher values of masses, but it is large for lower values of masses. Thus, a large mass range can be detected simultaneously for higher values of masses in a small spatial separation.

3.2. Simulations

Ion simulations using SIMION 7.0 were used to model the trajectory of ions as they propagate through the apparatus. These simulations have also guided us toward optimal conditions for our setup as graphically illustrated in Fig. 3. Simulations are shown for ions representing xenon's nine natural isotopes (from 124 to 136) and a low-mass range of mass-to-charge ratio (m/z) from 33 and 42. The starting positions resemble that of a typical ionization volume, where the initial displacement from the central axis was set at $\delta x = 3.0$ mm and $\delta z = 0.5$ mm along the axis. In this simulation, Xe ions are accelerated through the multi-lens velocity mapping assembly (4000/3200/1385 V/ground) and then 8.985 μs after laser ionization, a pulse of 750 ns duration and ±125 V is applied perpendicular to the flight direction. The range of the low-mass region, however, is simulated under slightly different conditions: 4.645 μs delay, 750 ns width and ±50 V orthogonal pulsed field. We use a simple square pulse controlled by user programming of the simulation so that rise and fall times of electric pulsers is not considered. Fig. 4 shows a plot of the transverse velocity (v_z) components as a function of the mass-to-charge ratio calculated at the pulse turn-off time (t_{off}) after receiving the orthogonal pulsed electric field. We fit the peaks in Fig. 4 with Eq. (7) and use the average peak positions from the transverse velocity distributions. In both cases, all the peaks are nicely fitted in terms of two mass-dependent contributions as we expect from Eq. (7). As a consequence, as ions experience more transverse pulsed field depending on the mass-to-charge ratio, they are forced more off-axis. After leaving the deflection region, therefore, ions start to separate spatially in the transverse direction according to mass-to-charge ratio. The magnitude of the dispersion is then greatly enhanced through the field free regions and the reflectron owing to the velocity mapping condition. After passing through the reflectron, ions of different mass finally impact upon a position sensitive detector, as shown in the lower left portion of Fig. 3. It is immediately apparent that the nine isotopes of Xe ions are visible as narrow spots, along a line, showing well-maintained velocity mapping conditions, and clearly separated in distinct region the plane of detector. From the extensive ion trajectory simulations, we find the ideal mass resolution is approximately 2600 for mass 132 (m/z) evaluated as the distance between two adjacent peaks divided by the full peak width at the measurement position. However, it should be noted that this value was obtained without considering the possible experimental error sources such as inhomogenous electric field, misalignment of ion optics or deflection plates, sensitivity of the detector, initial angular divergence of the atomic beam and distortion of ion trajectories due to the actual grid of the reflectron. Thus, it has to be regarded as an upper limit.

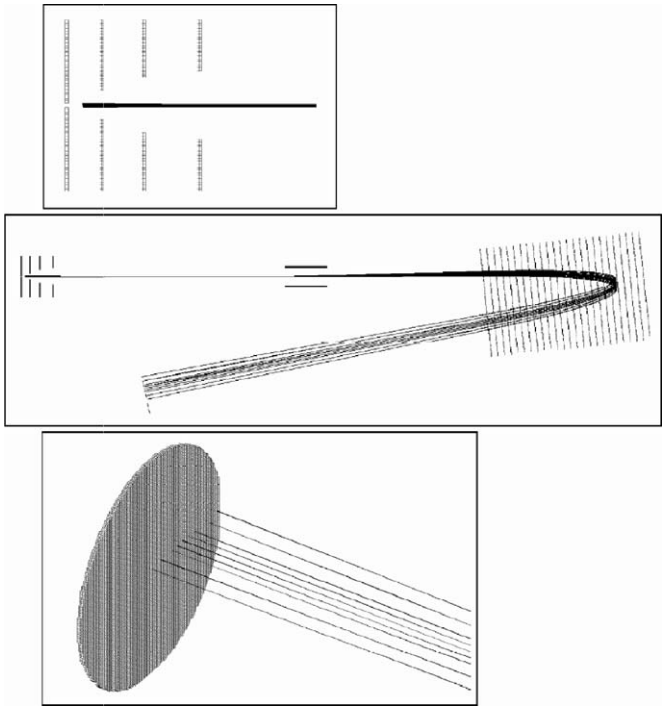

Fig. 3. Ion trajectory simulation for Xe isotopes using SIMION 3D 7.0. The insets demonstrate the initial distributions of Xe isotopes at the starting point and the spatial mass dispersion on a two-dimensional position sensitive detector.

3.3. Experimental results

Fig. 5A presents a spatially resolved image of the Xe isotope distribution obtained by resonant ionization of xenon. Each spot is clearly separated along the plane of detector and represent the natural abundance of Xe isotopes just as in the simulation. Although two isotope masses of the left side of image corresponding to $m/z = 124$ (0.09% natural abundance) and 126 (0.09% natural abundance) are difficult to visualize, the intensity distribution for the image can be plotted as a function of the pixel position, shown in Fig. 5B. By directly integrating each spot, we can measure the natural abundances of all nine Xe isotopes. The relative ratios agree well with literature values [21] as shown in Table 1. Event counting of the ion impacts easily yields dynamic ranges exceeding 10^3, and this is by no

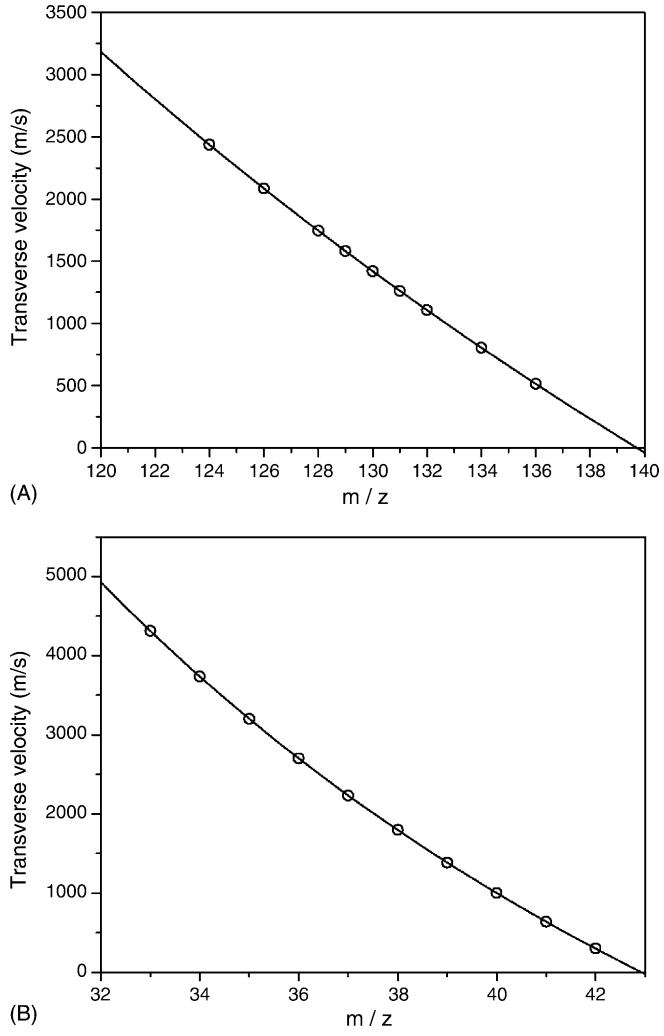

Fig. 4. The simulated transverse velocities as a function of mass-to-charge ratio at turn-off time of pulsed electric field for Xe isotopes (A) and range of mass from 33 to 42 (B), respectively. The solid lines were fitted with Eq. (7).

means a limit. The mass resolution was measured to be about 600 for $m/z = 132$, at full width half maximum (FWHM), which is the most abundant isotope in Xe. Fig. 6 shows the result of fitting experimental peak positions on the detector from the image in Fig. 5 to the expression in Eq. (9), while the plot of inset

Table 1
The measured relative abundance of Xe isotopes

Symbol	Mass of Xe atom	Natural abundance (%)	
		Reference value	This work
^{124}Xe	123.905896	0.09	0.10 (±0.04)
^{126}Xe	125.904269	0.09	0.09 (±0.04)
^{128}Xe	127.903530	1.92	2.03 (±0.21)
^{129}Xe	128.904779	26.44	26.15 (±0.46)
^{130}Xe	129.903508	4.08	4.60 (±0.41)
^{131}Xe	130.905082	21.18	21.68 (±0.50)
^{132}Xe	131.904154	26.89	25.92 (±0.67)
^{134}Xe	133.905395	10.44	10.55 (±0.31)
^{136}Xe	135.907220	8.87	8.87 (±0.49)

Uncertainties represent a single standard deviation for 15 images.

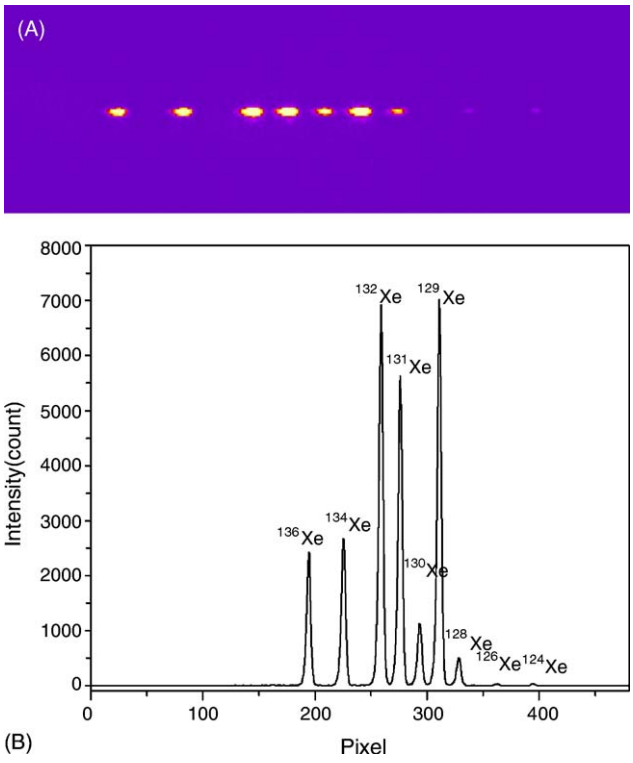

Fig. 5. (A) A spatially resolved image of nine Xe isotopes obtained by laser ionization in 300 × 100 pixels. (B) The intensity distribution for the image as a function of the pixel position.

represents a similar plot for the trajectory simulations. Both experimental and simulated data for Xe are quite well reproduced by Eq. (9) derived from simple theoretical considerations. Even though the mass resolving power is less than that of the ion trajectory simulations, our preliminary results are show that it is possible to achieve spatial mass dispersion simultaneously on a two-dimensional imaging detector with a simple pulsed field and velocity mapping conditions. Compared to conventional magnetic or electrostatic energy analyzer mass spectrometers

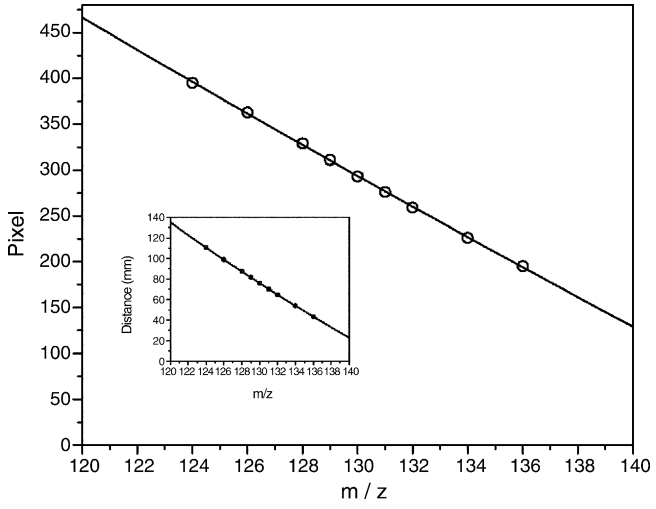

Fig. 6. The plot of experimentally measured positions by pixel as a function of mass-to-charge ratio of Xe isotopes while inset represents the simulated result. The solid lines were fitted with Eq. (9).

in particular, one of advantages of this design is that it is not necessary to place an imaging detector at the focal plane of magnet. In addition to the convenience and multiplex advantage associated with recording the entire measurement in a single image, for the experiments described here accurate abundance ratios can be obtained without the need for careful normalization or shot-to-shot comparisons. Finally, we envision the use of orthogonal pulsed fields to achieve an imaging version of tandem mass spectrometry, with many potential applications.

Acknowledgments

This work was supported by the Director, Office of Science, Office of Basic Energy Sciences, Division of Chemical Sciences, Geosciences and Biosciences, of the US Department of Energy under contract DE-AC02-9810886 through the BNL LDRD program, and at Wayne State University under contract number DE-FG02-04ER15593.

References

[1] S.A. McLuckey, J.M. Wells, Chem. Rev. 101 (2000) 571.
[2] W. Mo, B.L. Karger, Curr. Opin. Chem. Biol. 6 (2002) 666.
[3] J.J. Thomson, Proc. R. Soc. Lond. 89 (1913) 1.
[4] F.W. Aston, Nature 105 (1920) 617.
[5] J.H. Barnes rIV., G.H. Hieftje, Int. J. Mass Spectrom. 238 (2004) 33.
[6] A.O. Nier, J.L. Hayden, Int. J. Mass Spectrom. Ion Phys. 6 (1971) 339.
[7] J.H. Beynon, D.O. Jones, R.G. Cooks, Anal. Chem. 41 (1975) 1734.
[8] M.P. Sinha, Array Detectors for Simultaneous Measurement of Ions in Mass Spectrometry, WO Patent 9,728,888, 1997.
[9] A.D. Appelhans, J.E. Delmore, J.E. Olson, Int. J. Mass Spectrom. 241 (2005) 101.
[10] S.-K. Tsai, C.-K. Lin, Y.T. Lee, C.-K. Ni, Rev. Sci. Instrum. 72 (2001) 1963.
[11] D.W. Chandler, P.L. Houston, J. Chem. Phys. 87 (1987) 1445.
[12] A.T.J.B. Eppink, D.H. Parker, Rev. Sci. Instrum. 68 (1997) 3477.
[13] D. Townsend, S.A. Lahankar, S.K. Lee, S.D. Chambreau, A.G. Suits, X. Zhang, J. Rheinecker, L.B. Harding, J.M. Bowman, Science 306 (2004) 1158.
[14] M.H. Kim, B.D. Leskiw, A.G. Suits, J. Phys. Chem. A 109 (2005) 7839.
[15] B.D. Leskiw, M.H. Kim, A.G. Suits, Rev. Sci. Instrum. 76 (2005) 104101.
[16] D.A. Dahl, Int. J. Mass. Spectrom. 200 (2000) 3.
[17] W. Li, S.D. Chambreau, S.A. Lahankar, A.G. Suits, Rev. Sci. Instrum. 76 (2005) 063106.
[18] W.C. Wiley, I.H. McLaren, Rev. Sci. Instrum. 26 (1955) 1150.
[19] M. Guillhaus, J. Mass. Spectrom. 30 (1995) 1519.
[20] D.A. Dahl, A.D. Appelhans, M.B. Ward, Int. J. Mass Spectrom. 189 (1999) 47.
[21] K.J.R. Rosman, P.D.P. Taylor, Pure Appl. Chem. 71 (1999) 1593.